



THE UNIVERSITY *of* EDINBURGH

Edinburgh Research Explorer

Skeletal and global mechanisms for the combustion of gases released by crushed forest fuels

Citation for published version:

Tihay, V, Santoni, P-A, Simeoni, A, Garo, J-P & Vantelon, J-P 2009, 'Skeletal and global mechanisms for the combustion of gases released by crushed forest fuels' *Combustion and flame*, vol 156, no. 8, pp. 1565-1575., 10.1016/j.combustflame.2009.05.004

Digital Object Identifier (DOI):

[10.1016/j.combustflame.2009.05.004](https://doi.org/10.1016/j.combustflame.2009.05.004)

Link:

[Link to publication record in Edinburgh Research Explorer](#)

Document Version:

Author final version (often known as postprint)

Published In:

Combustion and flame

General rights

Copyright for the publications made accessible via the Edinburgh Research Explorer is retained by the author(s) and / or other copyright owners and it is a condition of accessing these publications that users recognise and abide by the legal requirements associated with these rights.

Take down policy

The University of Edinburgh has made every reasonable effort to ensure that Edinburgh Research Explorer content complies with UK legislation. If you believe that the public display of this file breaches copyright please contact openaccess@ed.ac.uk providing details, and we will remove access to the work immediately and investigate your claim.



**Skeletal and global mechanisms for the combustion of gases released by
crushed forest fuels**

**VIRGINIE TIHAY^a, PAUL-ANTOINE SANTONI^a, ALBERT SIMEONI^a, JEAN-
PIERRE GARO^b AND JEAN-PIERRE VANTELON^b**

^a SPE– UMR 6134 CNRS, University of Corsica, Campus Grossetti, BP 52, 20250 Corte,
France

^b LCD – UPR 9028 CNRS, ENSMA, University of Poitiers, 1 avenue Clément Ader, Téléport
2 – BP 40109, 86961 Futuroscope Chasseneuil Cedex, France

Type of article: Full length

Corresponding author:

Virginie Tihay

SPE – UMR 6134 CNRS, University of Corsica, Campus Grossetti, B.P. 52, 20250 Corte,
France,

Phone: +33 495 450 121, Fax: +33 495 450 162,

E-mail address: *tihay@univ-corse.fr*

Shortened Title: Gas combustion modelling for forest fuels

Abstract:

This study aims to improve the description of the gas phase combustion in physical models of forest fire spreading. The current models liken the degradation gases of forest fuels to carbon monoxide burning in air, whatever vegetation species. The first part of the study was devoted to determine whether the degradation gases have to be considered accurately in forest fire modelling. A laboratory experimental apparatus was designed to study the influence of the degradation gases on the laminar flames from crushed forest fuels. Thanks to these experiments, the role of the degradation gases on the gas phase combustion was highlighted. The second part was dedicated to improve the combustion models of degradation gases. Using numerical methods, the transient equations for the conservation of mass, momentum, energy and chemical species were solved as well as the radiative transfer equation for a laminar flame. Skeletal and global combustion mechanisms, including the main degradation gases released by forest fuels, were tested. The numerical predictions were evaluated by means of the accuracy of temperature and flux distributions and of computational time. The skeletal mechanisms provide results close to the experiments. However, they require too long computational times in reason of the number of elementary reactions. The comparisons between observed and predicted temperatures by the global mechanisms point out that the model considering only carbon monoxide underestimates significantly the temperature in the fire plume. On the contrary, the results obtained with the global mechanism including both methane and carbon monoxide with an incomplete oxidation of methane are in good agreement with the experimental data. This global mechanism is reliable and time saving meeting the requirements to be included in physical models of forest fires.

Keywords: degradation gases; forest fuels; laminar flame; combustion modelling; skeletal mechanism; global mechanism.

Nomenclature

a	absorptivity
C_p	specific heat
CT	computational time
D	mass diffusivity
e	total energy
F	view factor
\vec{g}	acceleration due to gravity
h	heat transfer coefficient
$h_{f,\alpha}$	reaction heat
HHV	high heating value
I	radiant intensity
J	irradiance
LHV	low heating value
$\dot{M}_{f,\alpha}$	production term of species resulting from the decomposition of the solid fuel
N	number of species
p	pressure
\dot{Q}	volumetric heat source
q_r''	radiant heat flux
r	radial coordinate
\vec{r}	direction vector
\vec{R}	radiant heat flux
s	norm of the unit vector along the radiant intensity path
\vec{s}	unit vector along the radiant intensity path

S	flame surface
t	time
T	temperature
u	radial coordinate of velocity
v	axial coordinate of velocity
\vec{V}	velocity
Y	mass fraction of species
z	axial coordinate

Greek symbols

α	fuel packing ratio
λ	thermal conductivity
ΔH	heat of combustion of volatiles
ρ	density
$\bar{\tau}$	viscous stress tensor
σ	Stefan-Boltzmann constant
σ_f	surface-to-volume ratio
$\dot{\omega}$	mass rate of production
χ	radiant fraction

Subscripts

eff	effective
f	fuel
i	species i
j	species j
g	gas phase

1. Introduction

The understanding of the physical mechanisms that control the wildfire ignition and spreading constitutes a major objective for management purposes. Over the last sixty years, the scientific community has become increasingly involved in both modelling and experimental areas of forest fire science. Three types of modelling approaches have emerged [1]. The simplest models are the statistical ones which make no attempt to involve physical mechanisms [2]. The empirical models [3] are based upon the conservation of energy but they do not distinguish the modes of heat transfer. Finally, the physical models differentiate the various kinds of heat transfer in order to predict the fire behaviour [4-6]. Recently, the new generation of these models (called detailed models) tends to include more and more physical mechanisms [7-9]. However, the numerous sub-models, which describe the physics of the fire, need to be improved. The modelling of the gas phase combustion is generally realised with three different approaches. In the first one, the combustion is modelled with global rates and thermodynamic parameters describing the burning of the cellulose fuel [10]. The second approach considers reduced mechanisms [11-12]. However, they are rarely included in CFD codes. In the last one (and the most often used), the combustible part of the devolatilization products is considered to be carbon monoxide burning in air [6,9], whatever vegetation species. Thus, there is a need of a simple and reliable combustion mechanism, which could be included in physical models of forest fires. The aim of this work is to improve the understanding of the combustion of gases released by the thermal degradation of forest fuels and to propose a combustion mechanism, which could be incorporated in the future in a forest fire model. This study was performed in two steps:

- An experimental work was carried out to determine whether the degradation gases have to be considered precisely in the modelling of forest fires. The burning of

crushed fuels was studied using unsteady, axisymmetric, non-premixed laminar flames [13]. These flames ensure a good reproducibility of the experiments. And they point out the effects of combustion kinetics on the flames, which are often hidden by turbulence or by the influence of the surface-to-volume ratio driving the radiant and convective heat transfers between the flame and the vegetation. The distribution of temperature, the flame reaction rate, the radiant fraction as well as the mass loss were measured and compared. Moreover, the gases released by the six fuels were identified and quantified by using a tube furnace connected to gas chromatographs and hygrometer.

- A numerical study was performed to determine how the degradation gases have to be taken into account in the models of forest fires. Skeletal and global mechanisms were investigated to establish the most suitable one for predicting gas phase combustion as they induce less computational time than detailed reaction mechanisms (over hundred reactions and around 50 species). After determining a suitable composition of degradation gases for modelling the laminar flames, four skeletal mechanisms were studied to determine which one provides the best compromise between accuracy and computational time. Then, three global mechanisms were tested and compared to the selected skeletal mechanism to establish a reliable model containing as fewer reactions as possible. Finally, the predictions obtained with the most suitable mechanisms were compared to experiments.

The paper is organized as follows. In the second section, the experimental procedures are described. The experimental results on the burning of crushed forest fuels are presented in the third section. Then, the numerical method is exposed. Finally, the simulated results are compared to the experimental data and discussed.

2. Experimental devices

2.1 Fuel samples

All experiments were performed with six Mediterranean fuels involved in wildland fires: *Pinus pinaster* (PP), *Pinus halepensis* (PH), *Pinus laricio* (PL), *Erica arborea* (EA), *Cistus monspeliensis* (CM) and *Arbutus unedo* (AU). Pine needles and shrub leaves and twigs were collected in winter during a period of hydrous stress for vegetation. They were oven-dried at 60°C during 24 hours. Then, they were crushed and sieved to a particle size of 0.6-0.8 mm. To determine the main properties of the crushed fuels, different methods were used. Only a global description of this protocol is presented in the following and the reader can refer to [13] for more details. The surface-to-volume ratio was obtained with a granulometric analysis. The HHV (High Heating Value) and the LHV (Low Heating Value) were measured by calorimetric bomb. The thermal diffusivity at 200°C was calculated from the thermal conductivity measured with a hot disk technique and the specific heat obtained by DSC. Table 1 reports the properties of the fuel samples measured by these methods. Initially, the plants studied in this work have very different surface-to-volume ratios (between 3550 and 8290 m⁻¹). It leads to different combustion dynamics [14] as this parameter pilots the radiant and convective heat transfers between the flame and the vegetative fuels. To focus on the role of the degradation gases, the surface-to-volume ratio of the fuel samples was homogenised by crushing and sieving. According to Table 1, two sample groups can be now distinguished: the first one includes CM and AU with a surface-to-volume ratio about 7250 m⁻¹ whereas the second one contains the three pines and EA with a mean surface-to-volume ratio around 6400 m⁻¹. Thus, thanks to the crushing, the influence of the fuel geometry can be neglected for samples belonging to a same group. For the six crushed fuels, the heating values are close (between 17.7 and 20.0 kJ.g⁻¹ for the LHV and between 19.2 and 21.8 kJ.g⁻¹ for the HHV).

The highest heating value is obtained for EA followed by PL, AU, CM, PH and PP. Concerning the thermal diffusivity, the highest value is observed for CM and PH ($2.10 \cdot 10^{-7} \text{ m}^2 \cdot \text{s}^{-1}$) followed by EA, PL, PP and AU ($1.53 \cdot 10^{-7} \text{ m}^2 \cdot \text{s}^{-1}$). All these properties are used in the following to explain the flame behaviour observed during the experiments.

2.2 Burning experiment

The burning of the crushed fuels was performed with the experimental device presented in Fig. 1. To determine the most suitable sample shape, different configurations were tested. The most appropriated form was obtained for a sample with a diameter of 3.5 cm and a mass of 1.5 g. Thanks to this configuration, the heat transfers are sufficient to sustain the flame and the sample burning produces a single laminar flame over the fuel. The crushed samples were placed on a load cell in order to measure their mass loss. The ignition was carried out with 0.7 ml of ethanol uniformly spread on the sample. An array of 11 thermocouples was positioned above the crushed fuel along the flame axis every centimetre. The first thermocouple was situated 5 mm above the sample surface. A second array with 7 thermocouples (spacing equal to 5 mm) was located horizontally movable at different heights to obtain the temperature along the flame diameter. The thermocouples used were mineral-insulated integrally metal-sheathed pre-welded type K (chromel-alumel) pairs of wire with an exposed junction. At the exposed junctions, the wires were 50 μm in diameter. A fluxmeter (MEDTHERM 64P-02-24T) was used to measure the radiant heat flux emitted from the flame. Its range of sensitivity was from 0 to 0.2 W/cm^2 ($\pm 50\%$). The radiant heat flux transducer was equipped with a Sapphire window with a view angle of 150°C . The sensor was horizontally oriented and was placed 2 cm above the sample surface. The uncertainty in temperature, mass and flux measurements were respectively 0.4 %, 2.5 % and 3 %. A frequency equal to 100 Hz was chosen with regard to the time constant of the thermocouples

(50 ms). It involves an over sampling of the other measurements. Two visible cameras were located inside the room to observe the flame geometry (flame height and flame radius). The interested reader can refer to [13] for the detail of the image processing. The ambient temperature was 21°C and the relative humidity was 50 %. At least five repetitions were made to collect reliable data for each fuel.

2.3 Gas analysis

The composition of the gases released by the fuels during their thermal degradation was determined with a tube furnace apparatus used as pyrolyser under nitrogen [13]. The study was only performed between 280 and 430°C to represent the burning condition of the crushed fuels during their combustion. The gas mixtures released during this range of temperature were collected into gas samplers connected either to a hygrometer (EdgeTech Model 2001 Series DewPrime) to quantify the water fraction or to gas chromatographs (Flame Ionization Detector and Thermal Conductivity Detector). An activated alumina column was used with a Flame Ionization Detector (FID) for hydrocarbons possessing less than four carbons. Helium was chosen as carrier gas with a flow rate of 30 ml.min⁻¹. A dual column packed with Porapack Q and a molecular sieve 5A was used with a Thermal Conductivity Detector (TCD) for O₂, CO and CO₂. The carrier gas was helium at 22 ml.min⁻¹. A column packed with a molecular sieve 13X was used with a TCD for H₂. The carrier gas was argon with a flow rate equal to 20 ml.min⁻¹. For the three columns, an isotherm was carried out at 50°C during 18 min 30. Then, a temperature increase with a heating rate of 8°C.min⁻¹ was set until 110°C. Finally, an isotherm at 110°C was performed during 21 min. The identification of the gases was managed by comparison with authentic standards. Their quantification was based on peak areas.

3. Experimental results

3.1 Combustion regimes

Two combustion regimes were observed during the burning of the crushed samples: the flickering and the laminar stages depending on the presence or the absence of ethanol.

- During the first 60 s after the ignition, the flame flickered (Fig. 2.a.). Frequency domain analyses of temperature profiles between 0 and 60 s showed indeed an 8 Hz predominant frequency. According to [15], this frequency is characteristic to the burning of ethanol. This stage corresponds to the first combustion regime called flickering stage. During this period, the flame height was up to 4 cm. The mass loss was the most significant (Fig. 3.a). It corresponds to the burning of ethanol with some sample degradation involved by the temperature increase in the crushed fuels. The highest mass loss is observed for CM followed by AU, EA, PH, PL and PP. By neglecting the char combustion, the energy conservation equation for solid fuel particles can be written as follows:

$$\alpha \rho_f C_{pf} \frac{dT_f}{dt} = \lambda_{eff} \Delta T_f + h \alpha \sigma_f (T - T_f) + \frac{\alpha \sigma_f}{4} (J - 4\sigma T_f^4) - \sum_{\alpha} \dot{M}_{f,\alpha} h_{f,\alpha} \quad (1)$$

The mean penetration distance $4/(\alpha \sigma_f)$ was 1.2 mm, 1.3 mm, 1.4 mm, 1.6 mm, 1.7 mm and 1.7 mm for AU, EA, PL, PP, PH and CM respectively. The radiation emitted by the flame entered in the crushed samples only on the first millimetres. The temperature in the fuel depended also on the conductive and convective heat transfers and to the re-radiation of the particle, which were strongly piloted by the surface-to-volume ratio of the particles. Thus, the high surface-to-volume ratio of CM and AU (Table 1) induced a higher mass loss than those of the other fuels. It explains the short burning time of CM and AU (between 110 and 130 s after the ignition).

- After 60 s, the 8 Hz frequency vanished. Ethanol was completely burned and the fuel was only composed of the degradation gases. This period corresponds to second stage. The mass loss was less significant than during the first stage (Fig. 3.b). The flame became laminar, axisymmetric and quite conical (Fig. 2.b.). For the three pines and EA, the burning time was up to 180 s and the laminar stage can be divided in two sub-stages: the regression and the extinction stages of the flame. The change between these extinction stages was characterized by an inflexion point on the mass burning rate curves (Fig. 3.b). During the regression stage, the flame height and the flame diameter decreased slowly. The highest mass burning rate was obtained by PH followed by EA, PL and PP. As the surface-to-volume ratio and the shape of the particles were close for these fuels, this behaviour is due to the thermal diffusivity of the samples (Table 1). The mass burning rate is all the more significant as the thermal diffusivity is high. After 120 s, the flame extinguished progressively. The mass burning rate of the four fuels was low. A same decrease tendency was observed for the three pines whereas that of EA was quickly because of the tar production, which settled on the sample surface, reducing the mass loss.

After flame extinction, for the whole samples, the remaining solid phase was essentially made up of carbon at the surface of the sample with a certain amount of unburned fuel near the load cell. Contrary to the other samples, the particles of EA were covered by tar.

3.2 Degradation gases

Table 2 shows the degradation gases analysed for the six fuels. They mainly consist of CO₂, CO, CH₄, H₂O, C₄H₆ and lower values of C₂ and C₄ hydrocarbons. These results are in agreement with literature [6]. All these gases mainly come from the degradation of the lignocellulosic compounds and in particular from the pyrolysis of cellulose and hemicellulose [16-

18]. The degradation products released by PP contain more combustible gases (about 27.1 %) than the other species. In the opposite, AU has the lowest amount of combustible (about 22.3 %). The highest content of water (about 13.8 %) is observed for CM whereas the lowest value is obtained for EA (4.7 %). Although the same gases are released by the six samples, the composition changes according to the fuels. The influence of these differences on the flames will be studied hereafter.

3.3 Flame characteristics

The radiant fraction emitted by the flame χ was calculated during the laminar with a solid-flame model:

$$\chi = \frac{S \cdot q_r''}{F \cdot \dot{m} \cdot \text{LHV}} \quad (2)$$

q_r'' represents the radiant heat flux measured with the fluxmeter at 11 cm from the flame axis. It allows considering an isotropic flux distribution. The view factor F was computed numerically by assuming that the flame was conical (Fig. 2.b). S , \dot{m} and LHV correspond to the flame surface, to the mass burning rate (Fig. 3) and to the low heating value of the sample (Table 1), respectively. CM and AU were not considered as they were at the end of their burning during the laminar stage (Fig. 3). The mean radiant fractions obtained by the four fuels were equal to 0.27, 0.24, 0.22 and 0.20 respectively for PP, PL, PH and EA. According to [19], the radiative fraction obtained for fuels with mixed saturated and unsaturated aliphatic and aromatic bounds between C, H, O, N and S is between 0.30 and 0.40 for fully ventilated turbulent combustion. Under laminar flow, radiant fractions are also lower than for turbulent conditions. Apart from the flow condition, the radiative fraction is affected especially by the fire size, the ventilation and the types of atoms and nature of chemical bonds in the fuel structure. In our experiments, the fire size and the ventilation were almost the same for the

four fuels. The only change came from the fuel nature. Thus, the differences observed among the radiative fractions of vegetative fuels can be attributed to the composition of their degradation gases.

The determination of the flame reaction rate per unit of flame surface was performed by drawing the lateral flame surface versus the mass flow rate of the degradation gases (Fig. 4). The char combustion was neglected (very little ash appeared at the surface of the fuel samples) and the mass flow of the degradation gases was assumed to be equal to the mass burning rate of the fuel samples (Fig. 3.b). The flame surface was calculated with the flame height and the flame radius below the smoke point [13] by assuming that the flame was conical. According to Fig. 4, the flame surface is proportional to the mass flow rate of the degradation gases except during the extinction stage, for which the mass flow rates is not significant. The inverse of this slope (between the flame surface and the mass flow rate) corresponds to the reaction rate per unit of flame surface. This value is also constant during the laminar regression stage but varies following the fuels. The highest reaction rates per unit surface are obtained for CM ($4.70 \text{ g.m}^{-2}.\text{s}^{-1}$) and AU ($3.60 \text{ g.m}^{-2}.\text{s}^{-1}$). Then, the crushed samples of pine needles have a similar behaviour with reaction rates equal to 1.98, 2.21 and $2.48 \text{ g.m}^{-2}.\text{s}^{-1}$ for PP, PH and PL respectively. Finally, EA have the lowest reaction rate per unit of flame surface with $1.20 \text{ kg.m}^{-2}.\text{s}^{-1}$.

Temperature distributions along the flame axis were compared for same mass flow rates and flame radiuses According to Fig. 5, the temperature profiles vary with the sample even if the behaviour of the solid phase is similar for each couple. The maximum of temperature appears around 1.5 cm high for PP whereas it is around 2 cm high for EA. It corresponds to a variation of 25 %. For AU, the temperature maximum is located at 1 cm high whereas it is at 2 cm for PL, representing a difference of 50 %. These behaviours are in agreement with the reaction rates. The higher the reaction rates per unit of flame surface are, the closer to the

surface sample is the combustion. Thus, the degradation gases influence the kinetics in the flame and modify its characteristics. The composition of the degradation gases must also be taken into account accurately in the combustion modelling to predict precisely the flames obtained from these crushed forest fuels.

4. Numerical model

The modelling of the experimental flames was conducted with Fluent during the laminar regression stage in order to test different combustion models. During this stage, the flames were indeed no more influenced by the ignition and were completely developed. Only the samples of the three pines and of EA were considered as CM and AU were at the end of their combustion.

4.1 Mathematical formulation

The model used was based on a detailed physical approach, which consists in solving the conservation equations (mass, energy, momentum) as well as the equations of radiation and transport for a laminar reacting flow. As we focused on the study of the gas phase combustion, the crushed fuel samples were represented by a burner [20]. This approximation was used as the crushed samples did not collapse during the burning and as the heterogeneous reactions in the sample can be neglected. According to these assumptions, the equations in the gas mixture can be written as follows:

$$\frac{\partial \rho}{\partial t} + \vec{\nabla} \rho \vec{V} = 0 \quad (3)$$

$$\frac{\partial \rho Y_i}{\partial t} + \rho \vec{V} \cdot \vec{\nabla} Y_i = \vec{\nabla} (\rho D_{ij} \vec{\nabla} Y_i) + \dot{\omega}_i \quad (4)$$

$$\frac{\partial \rho \vec{V}}{\partial t} + \rho \vec{V} \cdot \nabla \vec{V} = \nabla p + \rho \vec{g} + \nabla \cdot \vec{\tau} \quad (5)$$

$$\frac{\partial \rho e}{\partial t} + \rho \vec{V} \cdot \nabla e = \nabla \cdot (\lambda \nabla T) + \nabla \cdot \vec{R}_g + \nabla \cdot \left(\rho \sum_{i=1}^N h_i D_{ij} \nabla Y_i \right) - \nabla \cdot (p \vec{V}) + \nabla \cdot (\vec{\tau} \cdot \vec{V}) + \dot{Q} \quad (6)$$

$$\frac{dI(\vec{r}, \vec{s})}{ds} + aI(\vec{r}, \vec{s}) = a \frac{\sigma T^4}{\pi} \quad (7)$$

The properties (viscosity, density, thermal conductivity and diffusivity) of the gas species and of the gas mixture as well as the numerical methods were determined thanks to an analysis of parameterization and of sensitivity. The most efficient configuration in term of computational cost and accuracy was chosen. The Radiative Transfer Equation was solved by using the Discrete Ordinates Method [21]. The studied domain was discretized in 144 directions. To obtain a simple model for radiation, the gas was approximated by a mixture of grey gases containing CO₂ and H₂O as the flames were poorly sooty. For each gas species, the viscosity and the thermal conductivity were computed using the kinetic theory [22] whereas the specific heat capacity was a function of temperature. For the gas mixture, different laws were used. The density calculation was performed with an incompressible ideal-gas law. An ideal gas mixing law specified the viscosity and the thermal conductivity of the mixture. The diffusion coefficients were computed using the kinetic theory. A mixing law defined the specific heat capacity. The governing equations for the gas phase were solved with a non-uniform grid using a finite-volumes procedure. A first-order backward Euler scheme was used for time integration. Diffusion terms were approximated using a second-order central difference scheme. Convective terms were discretized using a second-order upwind scheme. The pressure-velocity coupling was handled by using the SIMPLE algorithm [23]. The resulting systems of linear algebraic equations were solved iteratively by using the Algebraic Multigrid

algorithm [24]. The modelling of the experimental flames during the laminar regression stage was performed on a 3.2 GHz dual processor workstation shipped with 2GB RAM.

4.2 Combustion mechanisms

An accurate description of the chemistry is possible thanks to detailed reaction mechanisms (over hundred reactions and around 50 species as the GRIMECH). However, this kind of mechanisms is time-consuming and is currently impractical in the physical detailed models for predicting the behaviour of wildfires because of the induced calculation time. Thus, the modelling of the oxidation of the degradation gases was performed with skeletal (SM) and global (GM) mechanisms. Four skeletal mechanisms were tested:

- The first skeletal mechanism (SM1) was elaborated by Leroy et al. [11] for the combustion of a gas mixture representative of the degradation gases released by forest fuels (CO, CH₄ and CO₂). It includes 49 reactions and 20 species and considers C₂ hydrocarbons.
- The second one (SM2) was created by Smooke and Giovangigli [25] for methane combustion. It is made up of 35 reactions and 17 species.
- The third mechanism (SM3) was developed by Peters and Kee [26] for methane oxidation. It is composed of 23 reactions and 14 species.
- The last skeletal mechanism (SM4) was proposed by Zhou and Mahalingam [12] for the combustion of degradation gases released by forest fuels. It contains 22 reactions and 14 species.

These mechanisms were elaborated from the GRIMECH. The main difference between these works was the composition of the degradation gases used for the test of the combustion

mechanisms. Only the study of Leroy et al. employed a gas mixture corresponding to the temperature measured in the sample during the burning experiments. The other works considered a higher pyrolysis temperature (around 1200 K).

Three combustion mechanisms, consisting of global reaction steps, were examined (the units used in the production rates are J, kmole, m³, second and Kelvin):

- The first global mechanism (GM1) only considers carbon monoxide. The CO oxidation produces CO₂ and the reverse reaction is taken into account:



The production rates of the chemical species were obtained thanks to Arrhenius's laws and were based on [27]. However, in this last work, the activation energy for carbon monoxide was developed for turbulent combustion and was not adapted for laminar flows. Thus, it was decreased until the combustion sustained. The reaction rates are given by:

$$\dot{\omega}_{\text{CO}} = 2.239 \cdot 10^{12} [\text{CO}] [\text{H}_2\text{O}]^{0.5} [\text{O}_2]^{0.25} \exp\left[-\frac{1.3 \cdot 10^8}{\text{R.T}}\right] \quad (9)$$

$$\dot{\omega}_{\text{CO}_2} = 5 \cdot 10^8 [\text{CO}_2] \exp\left[-\frac{1.3 \cdot 10^8}{\text{R.T}}\right] \quad (10)$$

- The second mechanism (GM2) takes into account carbon monoxide and methane. The combustion of carbon monoxide is identical to the previous case (Equations 8 to 10) while the oxidation of methane is given by:



with a production rate given by [27]:

$$\dot{\omega}_{\text{CH}_4} = 2.119 \cdot 10^{11} [\text{CH}_4]^{0.2} [\text{O}_2]^{1.3} \exp\left[-\frac{2 \cdot 10^8}{\text{R.T}}\right] \quad (12)$$

- The third mechanism (GM3) is a two-step global mechanism, which considers carbon monoxide and methane. The carbon monoxide is oxidized following equations 8 to 10 whereas the methane combustion is incomplete:



with a production rate given by [27]:

$$\dot{\omega}_{\text{CH}_4} = 5.012 \cdot 10^{11} [\text{CH}_4]^{0.7} [\text{O}_2]^{0.8} \exp\left[-\frac{2 \cdot 10^8}{\text{R.T}}\right] \quad (14)$$

4.3 Computational domain and boundary conditions

As the experimental flames were almost conical (Fig. 2.b), an axisymmetric condition was applied to decrease the computational time. Figure 6 presents the computational domain and the boundary conditions. The crushed sample was represented by the white rectangle on left-hand side of the domain. A Cartesian non-uniform grid covering a space domain of 11 cm × 15 cm was used. The grid contained 95 950 cells. The mesh size was equal to 0.2 mm along the vertical direction from $z = 0$ to 6 cm. Above 6 cm, a dilatation ratio of 1.03 was applied along the flame axis. Along the radial direction, the mesh size was 0.2 mm and 1 mm from $r = 0$ to 3.5 cm and from $r = 3.5$ to 11 cm, respectively. Several tests were performed to ensure that the size of the domain did not influence the flame behaviour and that the numerical results were grid-independent. The initial conditions of burner were taken from the inlet conditions. The mass flow inlet of the burner was fitted from the experimental mass flow rate. The radius of the burner, decreasing with time, was equal to the experimental flame

radius. The temperature of the gases was set to the mean value measured at the sample surface. The composition of the degradation gases released by the burner was based on the main gases analysed with the tube furnace (Table 2). For the air inlet, a pressure inlet condition was used to define the free boundary. The pressure was equal to the atmospheric pressure. The air flow was assumed to be normal to the boundary. The water fraction in most air was calculated from the experimental relative humidity ($Y_{\text{H}_2\text{O}} = 0.007$). At the top of the domain, pressure outlet was applied. All derivatives in the direction normal to the exit plane were assumed to be zero and the atmospheric pressure was prescribed. A stationary solution of the flow field was first computed without reaction. Then, the ignition was performed by applying a temperature of 1200 K near the burner. Finally, the computation of the flow field was performed by considering the combustion.

5. Numerical predictions

5.1 Composition of released gases

The whole gaseous species released by the forest fuels (Table 2) can not be considered in a simple oxidation model. The number of hydrocarbons has to be reduced and a modelled gas mixture must be determined. Two mixtures based on PL's analysis were used (Table 3) with the skeletal mechanism SM1. Mixture MC2 considers CO_2 , H_2O , CO , CH_4 and C_2 hydrocarbons whereas mixture MCH4 does not take into account C_2 hydrocarbons. The mass fractions of these species (except for CO_2) correspond to the values of Table 1 for PL. The mass fraction of CO_2 is taken to set the sum of all mass fractions equal to 1. The comparison of the gas composition was realised from the temperature distribution measured for PL, 60 s after ignition (beginning of the laminar stage). Figure 7 shows the results obtained along the

flame axis and radially at 0.5 cm high. The range of the experimental temperatures is represented by vertical lines. The addition of C₂ hydrocarbons in the gas mixture increases the maximal temperature around 100°C and shifts its position upwards (about 0.64 cm) and outwards (around 0.1 cm) respectively for the axial (Fig. 7.a) and the radial (Fig. 7.b) predictions. The simulations performed with MC2 over predict the experimental temperatures. The maximum temperature is higher than the experimental data and its position does not correspond to the experimental value. Conversely, the mixture MCH₄ provides a temperature distribution close to the experimental data in the flame. In the thermal plume, the predictions are slightly higher for the two mixtures. It could be due to the laminar modelling as the thermal plume becomes turbulent with height. The cooling of the fire plume due to the mixing with ambient air may thus be underestimated in comparison with the experiments. According to these results, the mass fractions of CO, CH₄ and H₂O must be directly equal to the measured values. The other combustible species have to be neglected in order to reproduce the combustion kinetics of our flames. In fire experiments [28], soot particles are produced and the reactions are incomplete. These phenomena were not considered here. Their consideration in the numerical model may modify the modelled gas mixture.

5.2 Skeletal mechanisms

Figure 8 presents a comparison of the temperatures predicted by the four skeletal mechanisms and mixture MCH₄ with the experimental data along the flame axis for PL at 60 s. The computational time of these mechanisms is provided in Table 4. The four temperature curves are very similar and close to the experimental results. Mechanism SM4 generates the highest temperatures and its curve presents an inflection point just before the maximum temperature. The predicted temperatures obtained with mechanisms SM1 and SM3 are very close.

Mechanism SM2 produces the lowest temperatures. The best agreement with the experimental results along the flame axis is obtained by this mechanism. Figure 9 illustrates the comparisons between temperature and species radial profiles at 0.5 cm high for PL at 60 s. Temperature profiles show that the temperature maximum predicted by SM2 is the highest following by SM3, SM1 and SM4. The location of the maximum of SM2 is shifted toward the oxidizer side whereas that of SM4 is moved toward the flame axis. The comparison of these results with the experimental data points out that mechanisms SM1, SM3 and SM4 provide predictions in the range of the experiments. Only mechanism SM2 induces a different combustion kinetics. For species profiles, the predictions of SM1 and SM3 are close. Some differences appear with SM4 for CH₄ and O₂ and with SM2 for CO. According to these results, it seems that mechanism SM1 and SM3 are the most accurate mechanisms. However SM3 has the advantage of a lower computational time. It is also the most suitable skeletal mechanism as it corresponds to the best compromise between the prediction accuracy and the computational time. However, in spite of this decrease, the computing time corresponds to twice duration required to compute the flow field without reaction.

5.3 Global mechanisms

To decrease again the computational time, global combustion mechanisms were investigated (Table 4). The simulations were based on the experiments of PL at 60 s. As mechanism GM1 does not take into account methane, two different mixtures called MCOa and MCOb (Table 3) based on mixture MCH₄ were considered. Mixture MCOa was established according to Grishin's hypothesis [6]. In this approach currently used in forest fire modelling [9], the mass fraction of CO is equal to the sum of the mass fractions of CO and CH₄. In mixture MCOb, the mass fraction of CO corresponds to the same Low Heating Value as mixture MCH₄. The mass fraction of CO₂ is taken to set the sum of all mass fractions equal to 1. To test

mechanism GM2 and GM3, mixture MCH4 was used. To insure that the predictions obtained with these mechanisms were correct, the temperatures were compared to the results of mechanism SM1 and to the experimental data. Figure 10 shows the experimental temperatures and the predictions obtained with the three global mechanisms and SM1 along the flame axis for PL at 60 s. The most considerable discrepancy is obtained by mechanism GM2. The temperature is significantly underestimated (about 200°C) and the combustion kinetics is badly reproduced. Mechanism GM1 with mixture MCOa does not produce better results as the temperature in the fire plume is badly described. The combination of mixture MCOb with mechanism GM1 provides better results. The temperature maximum is very close to that predicted by SM1. However, its position is closer to the burner (about 0.7 cm representing an error of 25 %). Thus, GM1 with MCOb does not predict correctly the combustion kinetics in the flame. Conversely, the results of mechanism GM3 are in agreement with the experimental data and predict accurately the combustion kinetics along the flame axis. Moreover, it provides results equivalent to SM1. The temperature maximum is only slightly lower (about 60°C) than that of SM1. Figure 11 illustrates the comparisons of temperature and species profiles calculated with SM1 and GM3 radially at 0.5 cm high for PL at 60 s. Temperature maxima of the two mechanisms are similar. Its location is however shifted toward the fuel side for mechanism GM3. The flame computed by GM3 tends to be tighter than that of SM1. The reaction zone is also closer to the flame axis shifting the temperature profiles towards the flame axis. For the two mechanisms, the temperature distributions are in the experimental range. The species evolution follows the same trend for both mechanisms. However, the CH₄ mass fraction obtained with GM3 is higher than that of SM1 whereas the mass fraction of CO is lower inside the flame. The global mechanism underestimates also slightly the conversion of CH₄ into CO. Concerning O₂, the consumption occurs closer to the fuel side for GM3. As for the temperature profile, it is due to the fact that the flame computed by the global

mechanism is tighter than that of SM1. Thus, thanks to the incorporation of methane and its incomplete combustion, mechanism GM3 provides a good approximation of the predictions performed by the skeletal mechanism SM1.

To ensure the accuracy of GM3, numerical predictions were performed for the other vegetative fuels. The temperature predictions and the experiments were compared along the flame axis (Fig. 12) and radially at 0.5 cm (Fig. 13) for PP, PH, PL and EA at 80 s. This time is inside the laminar stage and it corresponds to different mass flow rate and flame radius than those used for the preliminary study. The boundary conditions of the burner are summarized in Table 5. The gas compositions were based on Table 2 and mixture MCH4. The computed temperatures are in a good agreement with the experimental data. Along the flame axis, the predicted temperatures for PH, PL and EA are very close to the mean experimental measurements and remain in the experimental range in the flame zone. For PP, the temperature maximum is in agreement with the experiments. However, the results are shifted upwards. In this case, neglecting the soot seems not be suitable as the radiant fraction of this flame is high (0.27). In the thermal plume, the predictions for all fuels give a good order of magnitude of temperature even if they overestimate the experimental data because of the laminar flow modelling. Radially, the curves are characteristic of diffusion flames. Except for PP, for which the predictions are slightly shifted upwards, the temperature predictions are in the range of the experiments and the combustion kinetics is well reproduced.

To illustrate the radiant heat flux predictions obtained with GM3, the experimental and the computed radiant heat fluxes were compared for PL at 2 cm high for three positions of the radial direction and at different times of the laminar regression stage (at 60, 80 and 100 s, Fig. 14). For the three times, the flux predictions are close to the experimental data. The highest differences appear at 3.5 cm from the flame axis. But, they do not exceed $280 \text{ W}\cdot\text{m}^{-2}$ corresponding to less than 13 % of the experimental heat fluxes.

Thus, mechanisms GM3 provide in general a good representation of temperatures and radiant heat fluxes in the axisymmetric flame. Moreover, the use of this global mechanism, which considers only two reactions steps, decreases considerably the computational time as it is equal to the duration necessary to compute the flow field without reaction (Table 4). Mechanism GM3 matches also the two criteria established for the incorporation of a combustion mechanism in forest fire modelling: accuracy and low computational time.

6. Conclusions

This aim of this work was twofold. On one hand, it was devoted to the improvement of the understanding of the combustion of gases released by the thermal degradation of forest fuels. On the other hand, it intended to propose a simple and reliable combustion mechanism, which could be incorporated in a detailed model of forest fires. The work was conducted in two steps:

- Firstly, an experimental study was performed to determine the influence of the degradation gases on the flames of vegetative fuels. The gases released by six forest fuels were analysed. Different measurements (mass loss, temperature, radiant heat flux and flame reaction rate) were carried out on laminar flames obtained by the burning of crushed samples. These experimental data pointed out the role of the degradation gases on the combustion kinetics and also the necessity to take into account the degradation gases in forest fire models.
- Secondly, a combustion model able to predict the laminar flames of crushed forest fuels was defined. A modelled gas composition allowing predicting the flames was determined thanks to the skeletal mechanism of Leroy et al. [11]. It was composed of CO, CH₄, CO₂ and H₂O. Next, three other skeletal mechanisms were studied. We

determined that the mechanism of Peters and Kee (SM3) was the best compromise between accuracy and computational time. However, the computation time of this mechanism remains too long to be used in forest fire models. Then, global mechanisms were investigated as they induced no supplementary computational time. Mechanisms taking into account only carbon monoxide as a fuel provided bad predictions. This result put Grishin's hypothesis [6] in the wrong for laminar flames and underlines the necessity to improve the combustion mechanism. On the contrary, the global mechanism including both methane and carbon monoxide and considering an incomplete combustion of methane gave a good approximation of experimental temperatures and radiant heat fluxes for the four fuels.

This study constitutes also a first step, which must be followed by complementary works. Before incorporating this combustion model in forest fire models, it needs to be tested under turbulent conditions more representative of forest fires. To proceed, static and spreading turbulent fires will be investigated.

References

- [1] E. Pastor, L. Zárate, E. Planas, J. Arnaldos, *Prog Energy Combust Sci* 29 (2003), 139–153.
- [2] A.G. McArthur, *Weather and grassland fire behaviour*, Leaflet n°100, Australian Forest and Timber Bureau, 1966.
- [3] R.C. Rothermel, *A mathematical model for predicting fire spread in wildland fuels*, INT-115, USDA Forest Service, 1972.
- [4] F.A. Albini, *Combust. Sci. Tech.* 45 (1986) 101-113.
- [5] F. Morandini, A. Simeoni, P.A. Santoni, J.H. Balbi, *Comb. Sci. Tech.* 177 (2005) 1381-1418.
- [6] A.M. Grishin, *Mathematical Modeling of forest fires and new methods of fighting them*, Publishing House of the Tomsk State University, Tomsk, Russia, 1997, p. 390.
- [7] R.R Linn, *A transport model for prediction of wildfire behaviour*, University of California (UC-905), Los Alamos National Laboratory Report No. LA-13334-T, 1997.
- [8] A. Simeoni, P.A. Santoni, M. Larini, J.H. Balbi, J.H., *Fire Safety J.* 36 (2001) 491–513.
- [9] D. Morvan, J. L. Dupuy, *Combust. Flame* 138 (2004) 199-210.
- [10] X. Y. Zhou, J. C. F. Pereira, *Fire Mater.*, 24 (200) 37-43.
- [11] V. Leroy, E. Leoni, P.A. Santoni, *Combust. Flame* 154 (2008) 410-433.
- [12] X. Zhou, S. Mahalingam, *Combust. Sci. Technol.* 171 (2001) 39–70.
- [13] V. Tihay, A. Simeoni, P.A. Santoni, L. Rossi, J.P. Garo, J.P. Vantelon, *Int. J. Therm. Sci.* (2008) in press. J
- [14] .L. Dupuy, J. Maréchal, D. Morvan, *Combust. Flame*, 135 (2003) 65-76.
- [15] P.A. Santoni, T. Marcelli, E. Leoni, *Comb. Flame*, 131 (2002) 47-58.

- [16] R.H. White, M.A. Dietenberger, *Encyclop. of Mat. Sci. and Technol.*, (2001) 9712-9716.
- [17] S.L. LeVan, *Thermal degradation, Concise Encyclopedia of Wood and Woodbased Materials*, Pergamon, New York, 1989.
- [18] J.J.M. Orfão, F.J.A. Antunes, J.L. Figueiredo, *Fuel*, 78 (1999) 349-358.
- [19] A. Tewarson, *Generation of Heat and Chemical Compounds in Fires. SFPE Handbook of Fire Protection Engineering*, National Fire Protection Association, 2002.
- [20] V. Tihay, A. Simeoni, P.A. Santoni, J.P. Garo, J.P. Vantelon, *Combust. Sci. Technol.* 180 (2008) 1637-1658.
- [21] E.H. Chui, G.D. Raithby, *Num. Heat Trans*, 23 (B) (1993) 269-288.
- [22] H.A. McGhee, *Molecular Engineering*, McGraw-Hill, New York, 1991.
- [23] S.V. Patankar, *Numerical Heat Transfer and Fluid Flow*, Hemisphere Publishing Corporation, Washington, D.C., 1980.
- [24] B. R. Hutchinson, G.D. Raithby, *Num. Heat Trans*, 9 (1986) 511-537.
- [25] M. Smooke (Ed.), V. Giovangigli, *Reduced Kinetic Mechanisms and Asymptotic Approximations for Methane-Air Flames*, Springer-Verlag, Berlin, 1991, p.1.
- [26] N. Peters, R.J. Kee, *Combust. Flame*, 68 (1987) 17-29.
- [27] F.L. Dryer, I. Glassman, *Proc. Combust. Inst.*, 14 (1973) 987-1003.
- [28] T. Barboni, E. Leoni, D. Candelieri, X. Silvani, N. Chiaramonti, *Proc. 8th International Symposium on Fire Safety Science*, (2005) 1083–1093.

Table 1: Properties of the crushed fuel particles

Fuel	PP	PH	PL	EA	CM	AU
Surface-to-volume ratio σ_f (m^{-1})	6490	6080	6410	6760	7200	7400
Density ρ ($kg.m^{-3}$)	930	830	870	830	900	940
Fuel packing ratio α	0.39	0.39	0.44	0.45	0.33	0.45
HHV ($kJ.g^{-1}$)	19.2	19.9	20.8	21.4	19.8	20.2
LHV ($kJ.g^{-1}$)	17.7	18.3	19.3	20.0	18.4	18.8
Thermal diffusivity at 200°C ($10^{-7} m^2.s^{-1}$)	1.62	2.10	1.66	1.71	2.10	1.53

Table 2: Mass fractions of the degradation gases released between 280 and 430°C

Fuel	PP	PH	PL	EA	CM	AU
CO ₂	0.640	0.663	0.616	0.718	0.590	0.693
H ₂ O	0.089	0.070	0.074	0.047	0.138	0.084
CO	0.171	0.150	0.140	0.141	0.127	0.129
CH ₄	0.029	0.032	0.040	0.026	0.035	0.020
C ₂ H ₄	0.007	0.007	0.008	0.004	0.007	0.005
C ₂ H ₆	0.011	0.011	0.016	0.006	0.009	0.008
C ₃ H ₆	0.002	0.002	0.002	0.001	0.004	0.001
C ₃ H ₈	0.008	0.009	0.013	0.005	0.011	0.007
C ₄ H ₆	0.022	0.037	0.059	0.040	0.051	0.032
C ₄ H ₈	0.014	0.014	0.021	0.009	0.019	0.014
C ₄ H ₁₀	0.007	0.005	0.010	0.003	0.009	0.007
H ₂	0.000	0.000	0.001	0.000	0.000	0.000
O ₂	0.000	0.000	0.000	0.000	0.000	0.000

Table 3: Mass fractions of the gas mixtures used for the simulations of PL at 60 s.

Mixture	MC2	MCH4	MCOa	MCOb
CO ₂	0.616	0.746	0.746	0.588
H ₂ O	0.074	0.074	0.074	0.074
CO	0.140	0.140	0.180	0.338
CH ₄	0.040	0.040	-	-
C ₂ H ₄	0.008	-	-	-
C ₂ H ₆	0.016	-	-	-

Table 4: Computational time of the combustion mechanisms.

	SM1	SM2	SM3	SM4	GM1	GM2	GM3
Computation time (CT) (day)	7	3	3	3	1.5	1.5	1.5
Ratio between CT and DWR ¹	5	2	2	2	1	1	1

¹ DWR: Duration necessary to compute the flow Without Reaction (equal to 1.5 days on a 3.2 GHz dual processor workstation shipped with 2GB RAM).

Table 5: Boundary conditions of the burner used for the simulations at 80 s.

Fuels	PP	PA	PL	EA
CO	0.171	0.150	0.140	0.141
CH ₄	0.029	0.032	0.040	0.026
H ₂ O	0.089	0.070	0.074	0.047
CO ₂	0.711	0.748	0.746	0.787
T (°C)	460.5	324.9	413.5	481.7
Mass flow rate (mg.s ⁻¹)	2.83	4.90	3.00	3.15
Radius (cm)	1.58	1.48	1.25	1.61

List of Captions for the Figures

Fig. 1. Sketch of the experimental apparatus for the burning experiments.

Fig. 2. Flame shape during – a) flickering stage – b) laminar stage.

Fig. 3. – a) Mass in function of time – b) Mass burning rate during the laminar stage for PP, PH, PL and EA.

Fig. 4. Flame surface versus mass flow rate of the degradation gases during the regression and extinction stages.

Fig. 5. Mean temperature along the flame axis versus the vertical position for – a) PP and EA for a mass flow rate equal to 2.8 mg.s^{-1} - b) PL and AU for a mass flow rate equal to 3 mg.s^{-1} .

Fig. 6. Computational domain: a) grid – b) boundary conditions

Fig. 7. Comparison between experimental and numerical temperatures obtained with the two gas mixtures and the SM1 for PL at 60 s a) along the flame axis – b) radially at 0.5 cm high.

Fig. 8. Comparison of temperatures calculated with the skeletal mechanisms and the experimental data along the flame axis in the flame zone for PL at 60 s.

Fig. 9. Comparison of the temperature and the species distributions obtained with the skeletal mechanisms and the experimental temperatures at 0.5 cm high for PL at 60 s.

Fig. 10. Comparison of temperatures calculated with SM1 and the global mechanisms along the flame axis for PL at 60 s.

Fig. 11. Comparison of the temperature and the species distributions obtained with SM1 and GM3 and the experimental temperatures at 0.5 cm high for PL at 60 s.

Fig. 12. Comparison between experimental and numerical temperatures obtained with GM3 along the flame axis at 80 s for a) PP – b) PH – c) PL – d) EA.

Fig. 13. Comparison between experimental and numerical temperatures obtained with GM3 radially at 0.5 cm high at 80 s for a) PP – b) PH – c) PL – d) EA.

Fig. 14. Comparison between experimental and numerical heat fluxes obtained with SM3 and GM3 for PL at 2 cm high.

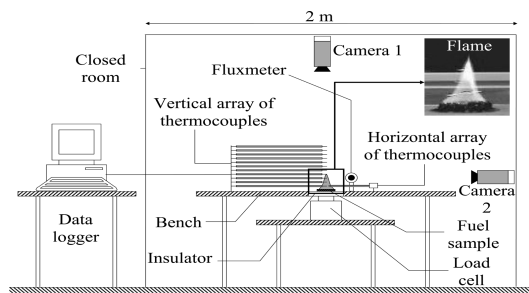


Fig. 1. Sketch of the experimental apparatus for the burning experiments.

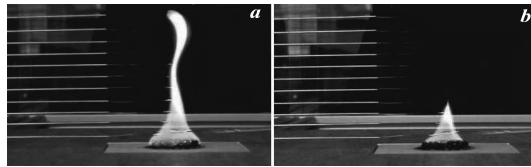


Fig. 2. Flame shape during – a) flickering stage – b) laminar stage.

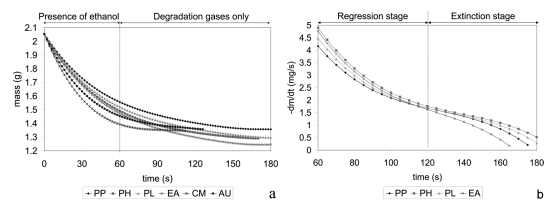


Fig. 3. – a) Mass in function of time – b) Mass burning rate during the laminar stage for PP, PH, PL and EA.

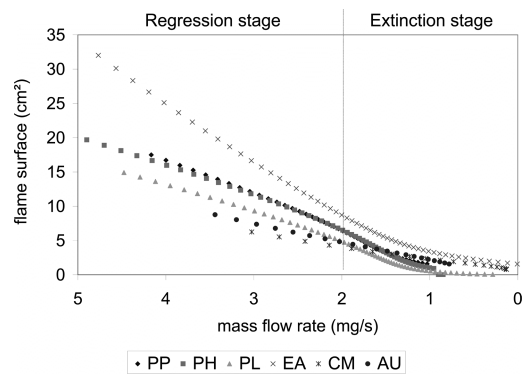


Fig. 4. Flame surface versus mass flow rate of the degradation gases during the regression and extinction stages.

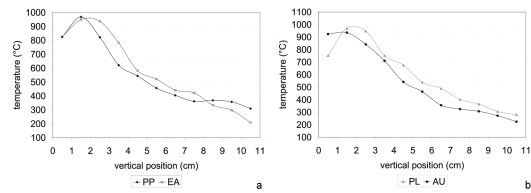


Fig. 5. Mean temperature along the flame axis versus the vertical position for – a) PP and EA for a mass flow rate equal to 2.8 mg.s⁻¹ - b) PL and AU for a mass flow rate equal to 3 mg.s⁻¹.

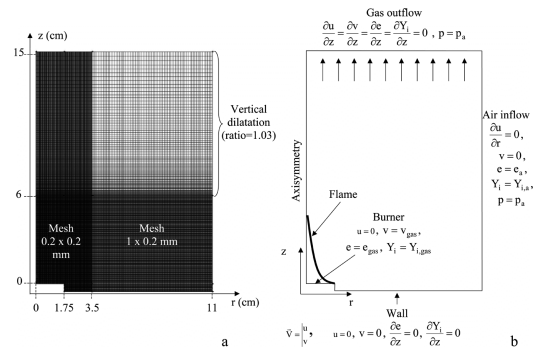


Fig. 6. Computational domain: a) grid – b) boundary conditions

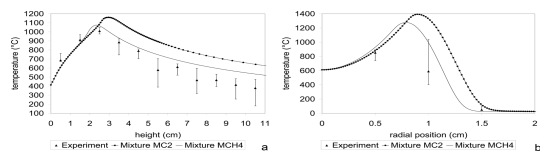


Fig. 7. Comparison between experimental and numerical temperatures obtained with the two gas mixtures and the SM1 for PL at 60 s a) along the flame axis – b) radially at 0.5 cm high.

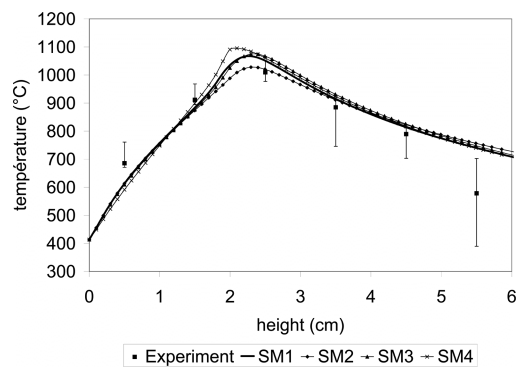


Fig. 8. Comparison of temperatures calculated with the skeletal mechanisms and the experimental data along the flame axis in the flame zone for PL at 60 s.

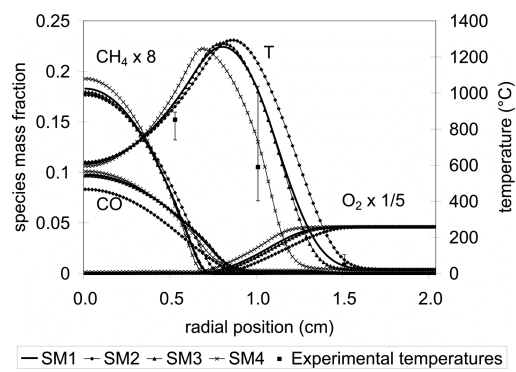


Fig. 9. Comparison of the temperature and the species distributions obtained with the skeletal mechanisms and the experimental temperatures at 0.5 cm high for PL at 60 s.

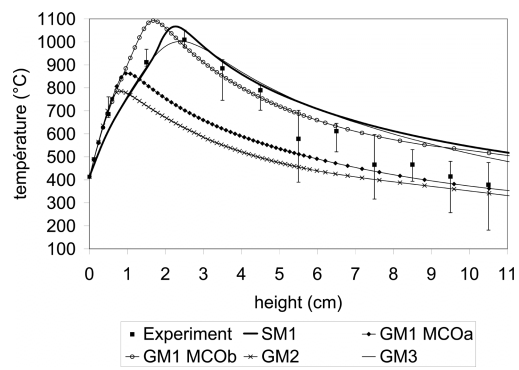


Fig. 10. Comparison of temperatures calculated with SM1 and the global mechanisms along the flame axis for PL at 60 s.

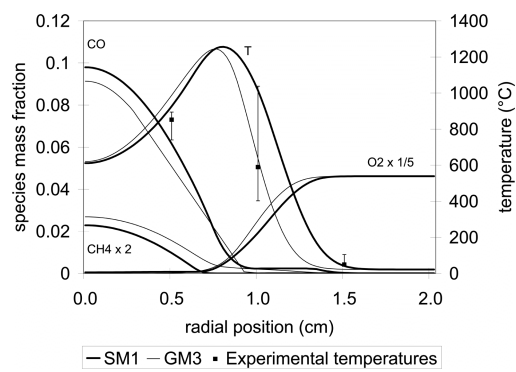


Fig. 11. Comparison of the temperature and the species distributions obtained with SM1 and GM3 and the experimental temperatures at 0.5 cm high for PL at 60 s.

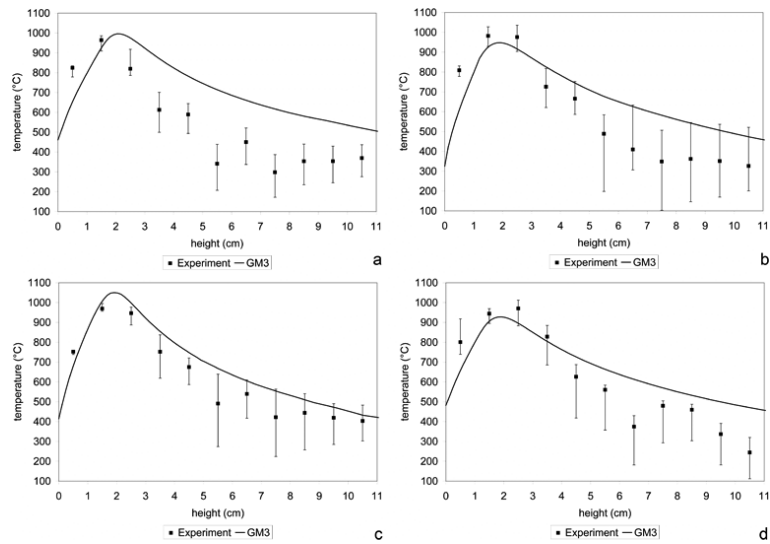


Fig. 12. Comparison between experimental and numerical temperatures obtained with GM3 along the flame axis at 80 s for a) PP – b) PH – c) PL – d) EA.

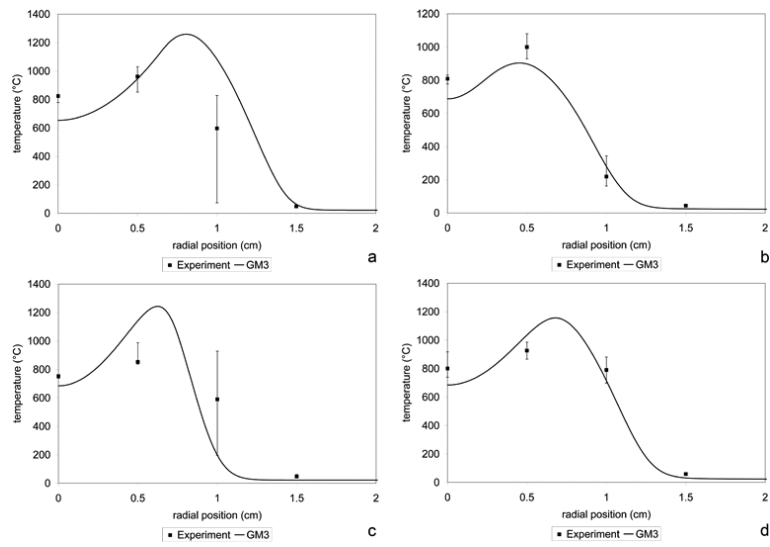


Fig. 13. Comparison between experimental and numerical temperatures obtained with GM3 radially at 0.5 cm high at 80 s for a) PP – b) PH – c) PL – d) EA.

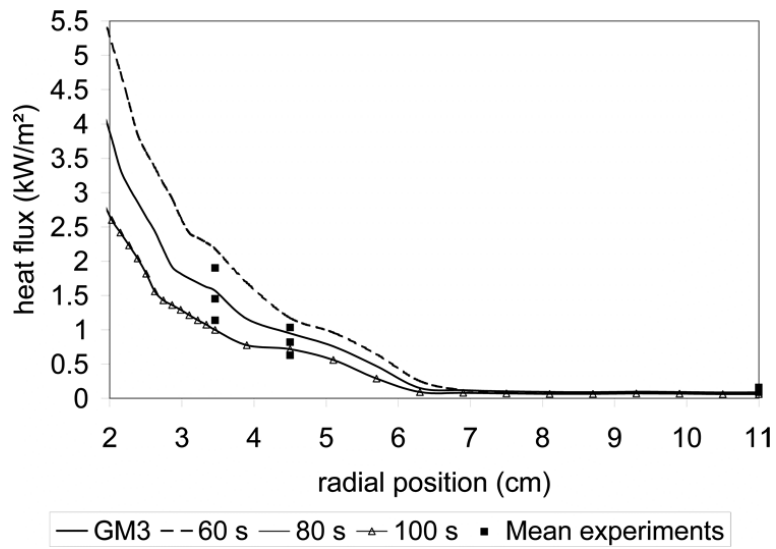


Fig. 14. Comparison between experimental and numerical heat fluxes obtained with GM3 for PL at 2 cm high.